

M. ŠILER
T. ČIŽMÁR
M. ŠERÝ
P. ZEMÁNEK✉

Optical forces generated by evanescent standing waves and their usage for sub-micron particle delivery

Institute of Scientific Instruments, Academy of Sciences of the Czech Republic,
Královopolská 147, 61264 Brno, Czech Republic

Received: 23 December 2005/Revised version: 29 March 2006
Published online: 16 May 2006 • © Springer-Verlag 2006

ABSTRACT Recently a non-contact organization of sub-micron colloidal particles in the vicinity of liquid–solid interface attracted great attention in connection with the development of imaging techniques using total internal reflection. We focus here on the theoretical description of the optical forces acting on a sub-micron particle placed in an interference field created by two counter-propagating evanescent waves. We study the behavior of nanoparticles by means of Rayleigh approximation, and also the behaviour of sub-micron particles by Lorentz–Mie scattering theory. Numerical results show how these forces depend on the particle size and angle of incidence of both beams. The alternating dependence on the bead size was proven experimentally, and the sub-micron beads behavior was experimentally studied in the motional evanescent standing wave. Self-organization of the beads into linear chains was also observed.

PACS 42.25.-p; 42.50.Vk; 82.70.Dd

1 Introduction

The light reflected under condition of total internal reflection creates evanescent field (EF) in the optically less dense medium. This field (also called near-field) only influences objects located very close to the prism surface. The significant feature of such a field is that it provides a two dimensional cut of sub-wavelength thickness, parallel to the surface of the prism, with the spatial variation of the field smaller than the illumination wavelength. The open access to the sample from the top in this geometry is very useful for facilitating practical applications. Additionally, one may obtain a field enhancement using surface plasmon resonances in a thin metal layer [1]. Approximately two decades ago all these properties led to the birth of a new type of optical microscopy with local probe – near field microscopy [2]. This area is also a topic of high interest in studies of negative refraction and superlensing [3]. In parallel with the evolution of optical microscopy there has been a proliferation of activity in optical trapping and manipulation methods [4]. This has resulted in widespread studies in biology, particularly of

molecular motors and has given new insights into colloidal science.

The use of radiative fields for confinement, manipulation and spatial organization of micro-objects is well-known and widely used [4]. However EF has not been a subject of intense investigation: Kawata et al. [5] observed that an EF created above a prism by total internal reflection caused guiding of polystyrene particles of micrometer size. In that paper the effects of an evanescent wave on the surface area of a diameter of 100 μm was studied. Subsequently, more work on the near field was performed, micron-size particles were guided along channelled waveguides [6, 7], spatial confinement of a 1–2 μm single polystyrene microsphere was demonstrated using an EF created by a TIR microscope objective [8]. Guiding or organization of many microparticles was reported over extended surface area of 1 mm [9], and nanoparticle confinement and even sorting were proposed by patterned optical near-field landscape [10]. Nanotip or nano-apertures were proposed for three-dimensional nano object confinement and manipulation [11–13]. A key attribute of the near field is the ability to organize particles over a very large area.

The interference of two counter-propagating evanescent waves creates an evanescent standing wave (ESW) above the surface. The standing wave provides better conditions for controlled axial particle localization due to strong gradients of the electric field intensity [14]. The whole ESW structure can be moved by altering the phase of one of the incident waves, resulting in a near-field optical conveyor belt (OCB). This is related to works in sliding standing waves using radiative fields which have been exploited for atom cooling and delivery using Gaussian beams [15, 16], or quite recently for sub-micron particle delivery using Bessel beams [17].

In this paper we present a method to calculate optical forces acting on a nanoparticle and a sub-micron particle placed into an EF created by two counter-propagating evanescent waves. With respect to the Rayleigh approximation used, we have to distinguish between Rayleigh particles (particle radius $a \ll \lambda/20$) and Mie particles (bigger). At the same time we describe an interferometric system that provides confinement and two-directional controllable delivery of particles of sub-micrometer sizes. Experimentally, we study how the velocity of ESW movement influences the behavior of a bead confined in the ESW.

✉ Fax: +420 541 514 402, E-mail: pavlik@isibrno.cz

2 Theory

We are especially interested here, in how the interference of several waves influences the behavior of a sub-micron particle in a liquid close to the liquid–prism interface. Therefore, we assume that the incident beams are linearly polarized plane waves that impact on a prism surface under the conditions of total reflection. The chosen plane waves, instead of using Gaussian beams, enabled considerable simplification of the analytical description which substantially decreased computational time but does not influence the principle physical conditions coming from the wave interference [18]. However, this approximation leads to the loss of all information about the behavior of a particle in the direction perpendicular to the beam axis and the plane of incidence. We have generalized the procedure given by Almaas [19] so that the incident field does not lie along one of the coordinate axes. Figure 1 shows the spatial configuration of the studied system illuminated by a plane wave coming from an arbitrary direction. The coordinate system is chosen so that the y -axis is perpendicular to the surface and the x -axis is perpendicular to the plane of incidence and lies on the surface. The field intensities of all waves are expressed in a joint coordinate system (base vectors \mathbf{x} , \mathbf{y} , \mathbf{z}). To calculate the field intensity of the j -th wave we introduce orthonormal coordinate systems ${}^j\mathbf{x}$, ${}^j\mathbf{y}$, ${}^j\mathbf{z}$, where ${}^j\mathbf{y}$ is identical to \mathbf{y} ; ${}^j\mathbf{x}$, ${}^j\mathbf{z}$ are parallel to the liquid–prism boundary; and ${}^j\mathbf{y}$ and ${}^j\mathbf{z}$ lie in the plane of incidence.

Furthermore, we will deal with an EF created by one incident plane wave (j -th). The prefix superscript identifying the wave is for simplicity omitted (in cases where possible). The intensity of the incident field in the prism of refractive index n_1 is $\mathbf{E}^{(1)}$; $E_{\parallel}^{(1)}$ is the field component lying in the plane of incidence (p -polarization) and $E_{\perp}^{(1)}$ is the normal component pointing in the positive ${}^j\mathbf{x}$ direction (s -polarization). The components $E_{\parallel}^{(2)}$ and $E_{\perp}^{(2)}$ of the electric field intensity $\mathbf{E}^{(2)}$ refer to the upper medium (liquid) with the refractive index n_2 . The angle of incidence of the plane wave is θ_1 .

In terms of unit vectors ${}^j\mathbf{x}$, ${}^j\mathbf{y}$, ${}^j\mathbf{z}$ we get at arbitrary point in the upper region

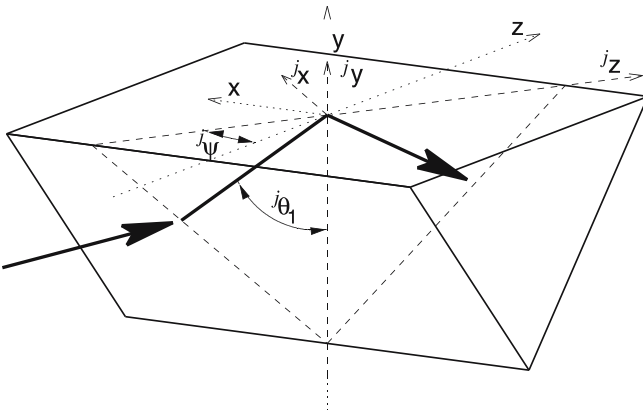


FIGURE 1 Orientation of a j -th incident plane wave and a prism. The incidence angle of the wave is ${}^j\theta_1$ and the plane of incidence is rotated by an angle ${}^j\psi$. The coordinate axes of the joint system and coordinate axis of the j -th wave are also shown

$$\mathbf{E}^{(2)} = {}^j\mathbf{x}E_{\perp}^{(2)} + {}^j\mathbf{y}E_{\parallel}^{(2)} \sin \theta_2 - {}^j\mathbf{z}E_{\parallel}^{(2)} \cos \theta_2, \quad (1)$$

where θ_2 is the refractive angle in the liquid. This angle is imaginary if $\mathbf{E}^{(2)}$ describes the evanescent wave. Let T_{\parallel} and T_{\perp} denote the ratio of the complex amplitudes of the field at the interface [19], i.e.

$$T_{\parallel} = \frac{E_{\parallel}^{(2)}}{E_{\parallel}^{(1)}} \Big|_{x=0}, \quad T_{\perp} = \frac{E_{\perp}^{(2)}}{E_{\perp}^{(1)}} \Big|_{x=0}. \quad (2)$$

In the case of total reflection, i.e. angle of incidence is bigger than critical angle, the ratios T_{\parallel} and T_{\perp} can be expressed in the following way

$$T_{\parallel} = \frac{2n_{21} \cos \theta_1}{n_{21}^2 \cos \theta_1 + i\sqrt{\sin^2 \theta_1 - n_{21}^2}}, \quad (3)$$

$$T_{\perp} = \frac{2 \cos \theta_1}{\cos \theta_1 + i\sqrt{\sin^2 \theta_1 - n_{21}^2}}, \quad (4)$$

where n_{21} is the ratio of the refractive index of the liquid and glass prism ($n_{21} = n_2/n_1$). The cosine and sine of the imaginary angle θ_2 taking place in (1) were expressed using Snell's law as follows:

$$\sin \theta_2 = \frac{1}{n_{21}} \sin \theta_1, \quad \cos \theta_2 = \frac{i}{n_{21}} \sqrt{\sin^2 \theta_1 - n_{21}^2}. \quad (5)$$

Furthermore, we introduce the following symbols

$$\beta = \frac{2\pi n_1}{\lambda} \sqrt{\sin^2 \theta_1 - n_{21}^2}, \quad \gamma = \frac{2\pi n_1}{\lambda} \sin \theta_1, \quad (6)$$

where β is the dumping factor in the evanescent region and γ is the wave number of the evanescent wave propagating in the ${}^j\mathbf{z}$ direction. The electric field intensity at an arbitrary point above the interface is

$$\mathbf{E}^{(2)} = ({}^j\mathbf{x}E_{0x} + {}^j\mathbf{y}E_{0y} + {}^j\mathbf{z}E_{0z}) \times \exp \varphi, \quad (7)$$

where

$$\begin{aligned} E_{0x}^{(2)} &= T_{\perp} E_{\perp}^{(1)}, & E_{0y}^{(2)} &= \frac{1}{n_{21}} T_{\parallel} E_{\parallel}^{(1)} \sin \theta_1, \\ E_{0z}^{(2)} &= -\frac{i}{n_{21}} T_{\parallel} E_{\parallel}^{(1)} \sqrt{\sin^2 \theta_1 - n_{21}^2}, \\ \varphi &= -\beta {}^j\mathbf{y} + i\gamma {}^j\mathbf{z}. \end{aligned} \quad (8)$$

Equations (7) and (8) describe the electric field in the coordinate system given by unit vectors ${}^j\mathbf{x}$, ${}^j\mathbf{y}$, ${}^j\mathbf{z}$. The field in joint coordinates given by vectors \mathbf{x} , \mathbf{y} , \mathbf{z} has the same formal shape (7) but with the components rotated by an angle ${}^j\psi$ along the y axis:

$$\begin{aligned} E_{0x}^{(2)} &= T_{\perp} E_{\perp}^{(1)} \cos \psi - \frac{i}{n_{21}} T_{\parallel} E_{\parallel}^{(1)} \sqrt{\sin^2 \theta_1 - n_{21}^2} \sin \psi, \\ E_{0y}^{(2)} &= \frac{1}{n_{21}} T_{\parallel} E_{\parallel}^{(1)} \sin \theta_1, \\ E_{0z}^{(2)} &= -T_{\perp} E_{\perp}^{(1)} \sin \psi - \frac{i}{n_{21}} T_{\parallel} E_{\parallel}^{(1)} \sqrt{\sin^2 \theta_1 - n_{21}^2} \cos \psi, \\ \varphi &= -\beta y + i\gamma x \sin \psi + i\gamma z \cos \psi. \end{aligned} \quad (9)$$

2.1 Forces acting on a Rayleigh particle

The time-averaged force acting on a so called Rayleigh particle (RP) having a radius a much smaller than the wavelength of the scattered light ($a \ll \lambda/20$) can be described analytically in a unified way using the following expression [20, 21]:

$$\langle F_{\xi} \rangle \equiv F_{\xi} = \frac{1}{2} \varepsilon_0 \varepsilon_m \operatorname{Re} \left\{ \sum_{\zeta=x,y,z} \alpha E_{\zeta} \frac{\partial E_{\zeta}^*}{\partial \xi} \right\}, \quad (10)$$

where $\xi = x, y$ or z , respectively; ε_0 is the permittivity of a vacuum, $\varepsilon_m \equiv n_2^2$ is the relative permittivity of the surrounding medium, Re means a real value of the expression in brackets, $*$ is the complex conjugate value and α is a complex valued polarizability of the object.

In the majority of previous studies concerning non-absorbing particles α was considered as real and expressed by a Lorentz–Lorenz formula (see (12)). In this case (10) gives only a so called gradient force [22]. Draine [23] showed that if the polarizability is a complex value in the form of (11), the field radiation reaction is taken into account and consequently the so-called scattering force is then an integral part of the expression given by (10)¹:

$$\alpha = \frac{\alpha_0}{1 + \frac{2}{3} \frac{ik^3 \alpha_0}{4\pi}} = \frac{\alpha_0}{1 + \frac{k^6 \alpha_0^2}{36\pi^2}} + i \frac{-\alpha_0^2 k^3}{6\pi \left(1 + \frac{k^6 \alpha_0^2}{36\pi^2}\right)}, \quad (11)$$

where $k = 2\pi n_1 \sin \theta_1 / \lambda_{\text{vac}}$ and α_0 is given by Lorentz–Lorenz relation:

$$\alpha_0 = 4\pi a^3 \frac{n_{32}^2 - 1}{n_{32}^2 + 2}, \quad (12)$$

where $n_{32} = n_3/n_2$ is the ratio of the refractive index of the particle n_3 and the surrounding medium n_2 . After substitution of (11) into (10) we obtain

$$F_i = \frac{1}{2} \varepsilon_0 \varepsilon_m \left[\alpha' \operatorname{Re} \left(\mathbf{E} \frac{\partial \mathbf{E}^*}{\partial x_i} \right) - \alpha'' \operatorname{Im} \left(\mathbf{E} \frac{\partial \mathbf{E}^*}{\partial x_i} \right) \right], \quad (13)$$

where Im means an imaginary value of the expression in brackets and α' and α'' are the real and imaginary parts of α . The force given by the first term in square brackets is a gradient force while the force given by the second term is a scattering force as discussed above. In the case of RP ($a \ll \lambda/20$) we get using (11), (12):

$$\alpha' \simeq \alpha_0, \quad \alpha'' \simeq -\frac{\alpha_0^2 k^3}{6\pi}, \quad \left| \frac{\alpha''}{\alpha'} \right| = \left| \frac{2m^2 - 1}{3m^2 + 2} (ka)^3 \right| \ll 1. \quad (14)$$

This result also shows that for RP the scattering force is much weaker than the gradient force.

¹ On the contrary to Draine we assume that the field time dependence is $\exp(i\omega t)$. Therefore we have to use addition instead of subtraction in the denominator of (11).

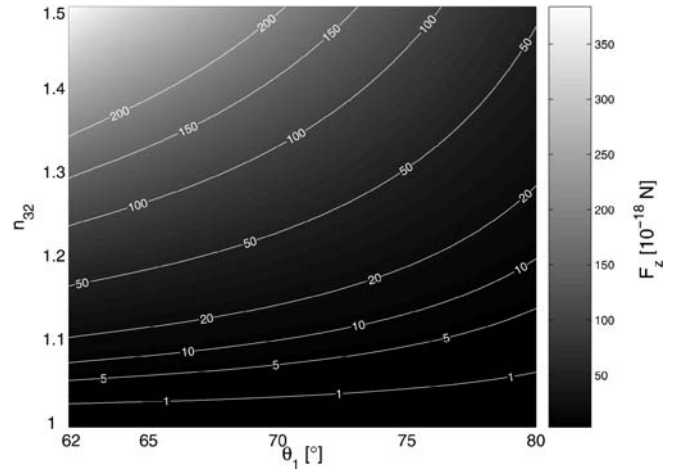


FIGURE 2 Force F_z acting on a nanoparticle (radius $a = 10$ nm) placed on the top of a prism (BK7 glass, $n_1 = 1.5098$) and illuminated by a single plane wave ($\lambda_{\text{vac}} = 532$ nm) linearly polarized perpendicular to the plane of incidence ($E_{\perp} = 1.8 \times 10^{12}$ V m⁻¹). The dependence on the angle of incidence θ_1 and the refractive index ratio $n_{32} = n_3/n_2$, $n_2 = 1.332$ (water) is studied

2.1.1 Single incident plane wave. The prism is illuminated by one plane wave, the electric field intensity of the evanescent wave is given by (7). We will assume that angle ψ is equal to zero, i.e. the coefficients taking place in (7) are given by (8). The resulting force acting on a particle is expressed as

$$\mathbf{F} = \frac{1}{2} \varepsilon_0 \varepsilon_m \alpha \times (\mathbf{x} F_{0x} + \mathbf{y} F_{0y} + \mathbf{z} F_{0z}) \times \exp(-2\beta y), \quad (15)$$

where $F_{0x} = 0$ and

$$\begin{aligned} F_{0y} &= -\beta |T_{\perp}|^2 E_{\perp}^2 - \frac{\beta}{n_{21}^2} |T_{\parallel}|^2 E_{\parallel}^2 (2 \sin \theta_1 - n_{21}^2), \\ F_{0z} &= -i\gamma |T_{\perp}|^2 E_{\perp}^2 - \frac{i\gamma}{n_{21}^2} |T_{\parallel}|^2 E_{\parallel}^2 (2 \sin \theta_1 - n_{21}^2). \end{aligned} \quad (16)$$

Figure 2 shows how the z -component of the force (F_z) acting on RP depends on the angle of incidence θ_1 and the refractive index ratio n_{32} . In Fig. 2 and all subsequent figures illustrating theoretical results, the amplitude of the electric field intensity is set to $E = 1.8 \times 10^{12}$ V m⁻¹. This value coincides with the electric intensity in the center of the Gaussian laser beam waist, the laser power is $P = 1$ W and the waist radius $w_0 = 1$ μ m.

2.1.2 Two counter-propagating plane waves. In this case the prism is illuminated by two counter-propagating plane waves ⁽¹⁾ \mathbf{E} and ⁽²⁾ \mathbf{E} . They have independent mutual polarizations and independent intensities of their electric fields. We also assume that these waves are coherent and interfere. The acting force calculated using (10) is given by (15) with

$$\begin{aligned} F_{0y} &= 2\beta n_{21}^2 [|T_{\perp}|^2 {}^{(1)}E_{\perp} {}^{(2)}E_{\perp} - |T_{\parallel}|^2 {}^{(1)}E_{\parallel} {}^{(2)}E_{\parallel}] \cos 2\gamma z \\ &\quad - \beta n_{21}^2 |T_{\perp}|^2 [{}^{(1)}E_{\perp}^2 + {}^{(2)}E_{\perp}^2] \\ &\quad - \beta |T_{\parallel}|^2 [{}^{(1)}E_{\parallel}^2 + {}^{(2)}E_{\parallel}^2] (2 \sin^2 \theta_1 - n_{21}^2), \\ F_{0z} &= 2\gamma n_{21}^2 [|T_{\perp}|^2 {}^{(1)}E_{\perp} {}^{(2)}E_{\perp} - |T_{\parallel}|^2 {}^{(1)}E_{\parallel} {}^{(2)}E_{\parallel}] \sin 2\gamma z \\ &\quad + i\gamma n_{21}^2 |T_{\perp}|^2 [{}^{(2)}E_{\perp}^2 - {}^{(1)}E_{\perp}^2] \\ &\quad + i\gamma |T_{\parallel}|^2 [{}^{(2)}E_{\parallel}^2 - {}^{(1)}E_{\parallel}^2] (2 \sin^2 \theta_1 - n_{21}^2). \end{aligned} \quad (17)$$

The y and z components of the force acting on RP have a sinusoidal dependence along the z axis. Figure 3 shows the dependence of the amplitude of force F_z on the angle of incidence θ_1 and the refractive index ratio n_{32} . One can see that the amplitude is several orders of magnitude larger than the force caused by the single wave. This is caused by the gradient force taking place in the counter-propagating waves instead of the scattering force in the single plane wave. If we neglect the contribution of scattering force to the total force given by (15), and (17), i.e. we neglect the imaginary part of F_{0z} , the resulting vectorial field is conservative and we define the potential U ($\mathbf{F} = -\nabla U$) as:

$$U = \frac{1}{2} \varepsilon_0 \varepsilon_m \alpha \times (-U_0 \cos 2\gamma z - U_1) \times \exp(-2\beta y), \quad (18)$$

where

$$U_0 = n_{21}^2 [|T_{\perp}|^{2(1)} E_{\perp}^{(2)} E_{\perp} - |T_{\parallel}|^{2(1)} E_{\parallel}^{(2)} E_{\parallel}],$$

$$U_1 = -\beta |T_{\parallel}|^2 [E_{(1)\parallel}^2 + {}^{(2)}E_{\parallel}^2] (2 \sin^2 \theta_1 - n_{21}^2).$$

The optical potential enables us to generally define the trap stiffness κ and trap depth ΔU . Let us focus only on the component along z axis for trap stiffness,

$$\kappa_z = \left| \frac{\partial F_z}{\partial z} \Big|_{z=z_{\text{eq}}} \right|, \quad (19)$$

where z_{eq} is the equilibrium position. In a sinusoidal potential we obtain

$$\kappa_z = 2\varepsilon_0 \varepsilon_m \alpha \gamma^2 U_0$$

$$= 2\varepsilon_0 \varepsilon_m \alpha \gamma^2 [|T_{\perp}|^{2(1)} E_{\perp}^{(2)} E_{\perp} - |T_{\parallel}|^{2(1)} E_{\parallel}^{(2)} E_{\parallel}]. \quad (20)$$

Trap depth is defined as the difference between the potential energy at the edge and the bottom of the optical trap which

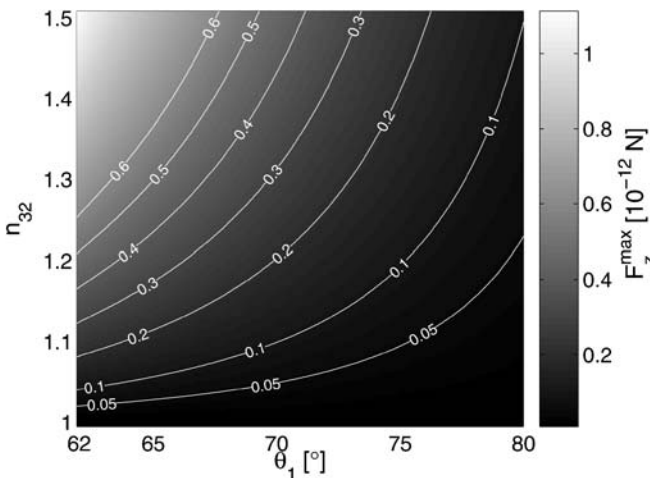


FIGURE 3 Amplitude of the z -component of force (F_z^{max}) acting on a nanoparticle (radius $a = 10$ nm) placed on the top of a prism (BK7 glass) and illuminated by two counter-propagating plane waves ($\lambda_{\text{vac}} = 532$ nm) linearly polarized parallel to the plane of incidence (${}^{(1)}E_{\parallel} = {}^{(2)}E_{\parallel}$ = 1.8×10^{12} V m $^{-1}$). The dependence on angle of incidence θ_1 and refractive index ratio n_{32} is studied. Both waves are incident under the same angle. Other parameters are the same as in Fig. 2

gives a sinusoidal potential

$$\Delta U = \varepsilon_0 \varepsilon_m \alpha U_0 = \kappa_z / (2\gamma^2). \quad (21)$$

2.2 Lorentz–Mie theory

Optical forces expressed within the Rayleigh approximation provide a useful insight into the behavior of nanoparticles in the interference evanescent field. However, Lorentz–Mie scattering theory has to be applied to predict the behavior of bigger particles. The optical forces acting on a spherical particle were presented by Barton et al. [24]. To calculate these forces it is necessary to express the coefficients A_{lm} and B_{lm} in the expansion of the radial component of the incident field to the spherical harmonics. The radial component of the field given by (7), and (9) can be expressed in a spherical coordinate system with its beginning at the center of the sphere (similarly to [19]):

$$E_r^{(2)} = E_x^{(2)} \sin \vartheta \cos \varphi + E_x^{(2)} \sin \vartheta \sin \varphi + E_z^{(2)} \cos \vartheta$$

$$= \left\{ T_{\perp} E_{\perp} (\cos \psi \sin \vartheta \cos \varphi - \sin \psi \cos \vartheta) \right.$$

$$\left. - \frac{1}{n_{21}} T_{\parallel} E_{\parallel} \left(i \sqrt{\sin^2 \theta_1 - n_{21}^2} \sin \psi \sin \vartheta \cos \varphi \right. \right.$$

$$\left. - \sin \theta_1 \sin \vartheta \sin \varphi + i \sqrt{\sin^2 \theta_1 - n_{21}^2} \cos \psi \cos \vartheta \right\}$$

$$\times \exp \{ -\beta a \sin \vartheta \sin \varphi + i \gamma a \sin \psi \sin \vartheta \cos \varphi$$

$$+ i \gamma a \cos \psi \cos \vartheta \}$$

$$\times \exp \{ -\beta y_0 + i \gamma \sin \psi x_0 + i \gamma \cos \psi z_0 \}, \quad (22)$$

where x_0 , y_0 and z_0 are coordinates of the sphere center, ϑ and φ are polar and azimuthal angles. The coordinates x , y , z were expressed using transformations

$$x = x_0 + a \sin \vartheta \sin \varphi,$$

$$y = y_0 + a \sin \vartheta \cos \varphi,$$

$$z = z_0 + a \cos \vartheta. \quad (23)$$

The radial component of the magnetic field can be derived using the same procedure:

$$H_r^{(2)} = \left\{ -n_{21} T_{\parallel} H_{\perp} (\cos \psi \sin \vartheta \cos \varphi - \sin \psi \cos \vartheta) \right.$$

$$\left. - T_{\perp} H_{\parallel} \left(i \sqrt{\sin^2 \theta_1 - n_{21}^2} \sin \psi \sin \vartheta \cos \varphi \right. \right.$$

$$\left. - \sin \theta_1 \sin \vartheta \sin \varphi + i \sqrt{\sin^2 \theta_1 - n_{21}^2} \cos \psi \cos \vartheta \right\}$$

$$\times \exp \{ -\beta a \sin \vartheta \sin \varphi + i \gamma a \sin \psi \sin \vartheta \cos \varphi$$

$$+ i \gamma a \cos \psi \cos \vartheta \}$$

$$\times \exp \{ -\beta y_0 + i \gamma \sin \psi x_0 + i \gamma \cos \psi z_0 \}. \quad (24)$$

We calculated the coefficients A_{lm} and B_{lm} for a unit amplitude of the incident wave and for bulk polarizations p and s , i.e. we calculate the dimensionless coefficients A_{lm}^{\perp} , A_{lm}^{\parallel} , B_{lm}^{\perp} and B_{lm}^{\parallel} . Coefficients A_{lm} and B_{lm} of the incident wave with arbitrary polarization are done as follows

$$A_{lm} = E_{\parallel} A_{lm}^{\parallel} + E_{\perp} A_{lm}^{\perp}; \quad B_{lm} = H_{\parallel} B_{lm}^{\parallel} + H_{\perp} B_{lm}^{\perp}. \quad (25)$$

To simplify the expressions of the coefficients A_{lm} and B_{lm} the following substitutions are used:

$$i\mathbf{k}_2\mathbf{r}_0 = -\beta y_0 + i\gamma \sin \psi x_0 + i\gamma \cos \psi z_0,$$

$$C_1 = \gamma a \cos \psi,$$

$$C_2 = a\sqrt{\gamma^2 \sin^2 \psi - \beta^2},$$

$$C_3 = \sqrt{\sin^2 \theta_1 - n_{21}^2},$$

$$\Phi = \operatorname{atanh}\left(\frac{\beta}{\gamma \sin \psi}\right),$$

$$\begin{aligned} Q_1^{lm} &= \int_0^{\pi/2} d\vartheta \sin^2 \vartheta P_l^m(\cos \vartheta) \begin{Bmatrix} \cos \\ i \sin \end{Bmatrix} (C_1 \cos \vartheta) \\ &\quad \times \{e^{-\Phi} J_{m-1}(C_2 \sin \vartheta) + e^{\Phi} J_{m+1}(C_2 \sin \vartheta)\}, \\ Q_2^{lm} &= \int_0^{\pi/2} d\vartheta \sin^2 \vartheta P_l^m(\cos \vartheta) \begin{Bmatrix} \cos \\ i \sin \end{Bmatrix} (C_1 \cos \vartheta) \\ &\quad \times \{e^{-\Phi} J_{m-1}(C_2 \sin \vartheta) - e^{\Phi} J_{m+1}(C_2 \sin \vartheta)\}, \\ Q_3^{lm} &= \int_0^{\pi/2} d\vartheta \sin \vartheta \cos \vartheta P_l^m(\cos \vartheta) \begin{Bmatrix} i \sin \\ \cos \end{Bmatrix} (C_1 \cos \vartheta) \\ &\quad \times 2J_m(C_2 \sin \vartheta), \end{aligned} \quad (26)$$

where $P_l^m(x)$ is the associated Legendre function, the symbols $\begin{Bmatrix} f_1 \\ f_2 \end{Bmatrix}(x)$ means that the function $f_1(x)$ or $f_2(x)$ are evaluated if $l+m$ is even or odd, respectively. The coefficient A_{lm}^{\parallel} is given as follows:

$$\begin{aligned} A_{lm}^{\parallel} &= \frac{-2T_{\parallel} i^m \pi e^{m\Phi}}{n_{21} l(l+1) \psi_l(k_2 a)} \exp(i\mathbf{k}_2\mathbf{r}_0) \sqrt{\frac{2l+1}{4\pi} \frac{(l-m)!}{(l+m)!}} \\ &\quad \times [\sin \theta_1 Q_1^{lm} + C_3 \sin \psi Q_2^{lm} + iC_3 \cos \psi Q_3^{lm}], \end{aligned} \quad (27)$$

where $\psi_l(x)$ is the Riccati–Bessel function and $k_2 = 2\pi n_2/\lambda$. The coefficient A_{lm}^{\perp} is given as follows:

$$\begin{aligned} A_{lm}^{\perp} &= \frac{-2T_{\perp} i^m \pi e^{m\Phi}}{l(l+1) \psi_l(k_2 a)} \exp(i\mathbf{k}_2\mathbf{r}_0) \sqrt{\frac{2l+1}{4\pi} \frac{(l-m)!}{(l+m)!}} \\ &\quad \times [i \cos \psi Q_2^{lm} + \sin \psi Q_3^{lm}]. \end{aligned} \quad (28)$$

The dimensionless coefficients B_{lm}^{\parallel} and B_{lm}^{\perp} can be calculated from coefficients A_{lm}^{\parallel} , A_{lm}^{\perp} using the following relations, see (22) and (24):

$$B_{lm}^{\parallel} = \frac{n_{21} T_{\perp}}{T_{\parallel}} A_{lm}^{\parallel}, \quad B_{lm}^{\perp} = -\frac{n_{21} T_{\parallel}}{T_{\perp}} A_{lm}^{\perp}. \quad (29)$$

The coefficients A_{lm} and B_{lm} given by (25), (27)–(29) describe an expansion of one wave incident on the bead to the spherical harmonics. The total coefficients including all incident waves are sums of these individual components. The convenient result derived from (26)–(29) shows that the dependence of coefficients A_{lm} and B_{lm} on the position of a bead center is given only by term of the $\exp(i\mathbf{k}_2\mathbf{r}_0)$ and does not depend on the indices l and m . Moreover it does not depend on polarization of the wave either. This property is used to accelerate the numerical computations. Figure 4 compares the forces acting on a particle calculated by the Lorentz–Mie and Rayleigh theory. The plot is shown for wave polarizations perpendicular to the plane of incidence. One can see that for F_y there is a good agreement between both theories even for bead sizes as big as 90 nm. This is not true for F_z where agreement within 10% occurs only for nanoparticles smaller than 20 nm ($a \approx \lambda/20$). Figure 5 shows the amplitude of force F_z acting on a Mie particle placed in the interference field, with dependence on the angle of incidence and the particle radius. One can see that there are certain sizes of beads that are not influenced by the standing wave while there are other sizes that are strongly influenced. Similar behavior has been observed in a standing Gaussian wave [25, 26], a weak Gaussian standing wave

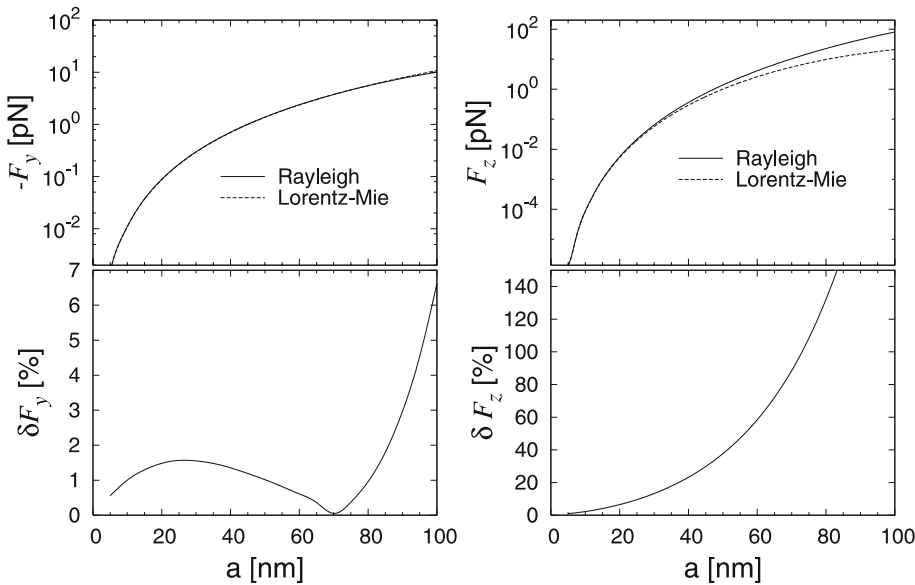


FIGURE 4 Comparison of forces acting on beads of different sizes calculated by Rayleigh and Lorentz–Mie theory. A polystyrene bead ($n_3 = 1.57$) in water on the top of a BK7 prism is illuminated by a plane wave ($\lambda_{\text{vac}} = 532$ nm) with polarization perpendicular to the plane of incidence and incidence angle $\theta_1 = 62^\circ$. Upper plots show y (left) and z (right) components of the force in a logarithmic scale (for the case of F_y the logarithm of the absolute value is plotted). The lower plots show the relative difference in % of values obtained by Rayleigh and Lorentz–Mie theories ($\delta F = |F_{\text{Rayleigh}} - F_{\text{Lorentz-Mie}}|/|F_{\text{Lorentz-Mie}}|$)

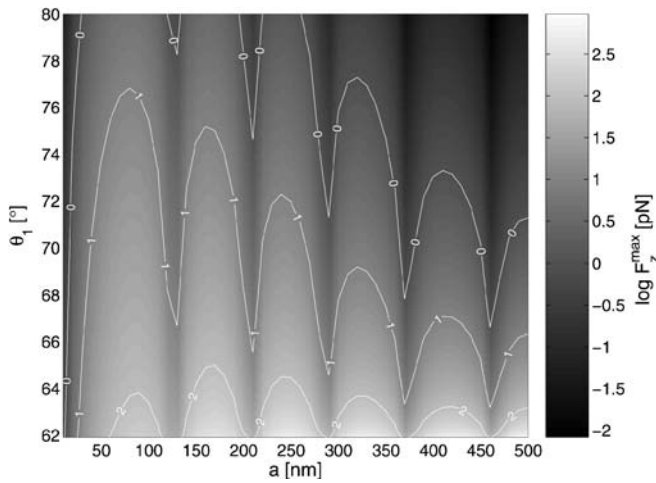


FIGURE 5 Decadic logarithm of amplitude of z component of force F_z^{\max} acting on a Mie particle placed in the interference field in dependence on the angle of incidence and particle diameter. Both waves are incident under the same angle θ_1 and they are polarized parallel to the plane of incidence ($^{(1)}E_{\parallel} = ^{(2)}E_{\parallel} = 1.8 \times 10^{12} \text{ V m}^{-1}$). Other parameters are the same as in Fig. 2. The *white contours* show the force amplitudes of 1, 10, and 100 pN

above the surface [27], and a Bessel standing wave [17]. This fact can be used for controllable sorting of particles according to their sizes [28].

3 Experimental results

Up to the present, the interference of counter-propagating evanescent waves was generated using a retro-reflecting mirror and it was used for generation of periodic light patterns for near-field microscopy experiments [29]. In contrast to those methods we used a setup with two independent counter-propagating Gaussian beams that were focused on the top surface of the prism. Tuning the incident angle may result in either a surface patterned evanescent field or a propagating light field just above the surface (see Fig. 6). Moreover this set-up enables us to alter the relative phase between the two beams in a controlled fashion by a movable mirror. Its movement results not only in the motion of the standing wave but also in the motion of objects confined in this standing wave. A recording of the light scattered by a moving bead with radius 100 nm is shown in Fig. 7. This was the smallest size of bead we succeeded in confining and delivering, and its movement over $5 \mu\text{m}$ is demonstrated. We have also used this optical conveyor belt (OCB) to deliver bigger beads and Fig. 8 shows experimentally how the size of the bead influences the bead sensitivity to the standing wave motion. The observed sensitivity to ESW motion coincides very well with theoretical predictions in Fig. 5. Therefore we chose only bead sizes sensitive to the ESW motion in the subsequent experiments.

In the subsequent part of this paper, we focus on the quantitative study of how the velocity of the standing wave influences the velocity of particle movement. At first we focus on the properties of a bead confined in the stationary ESW. The movement of a polystyrene particle (radius $a = 260 \text{ nm}$) was recorded by fast CCD camera (IDT X-Stream XS3, 4GB) recording 6120 fps over a period of 1 s. The position of the bead center was evaluated with subpixel accuracy by

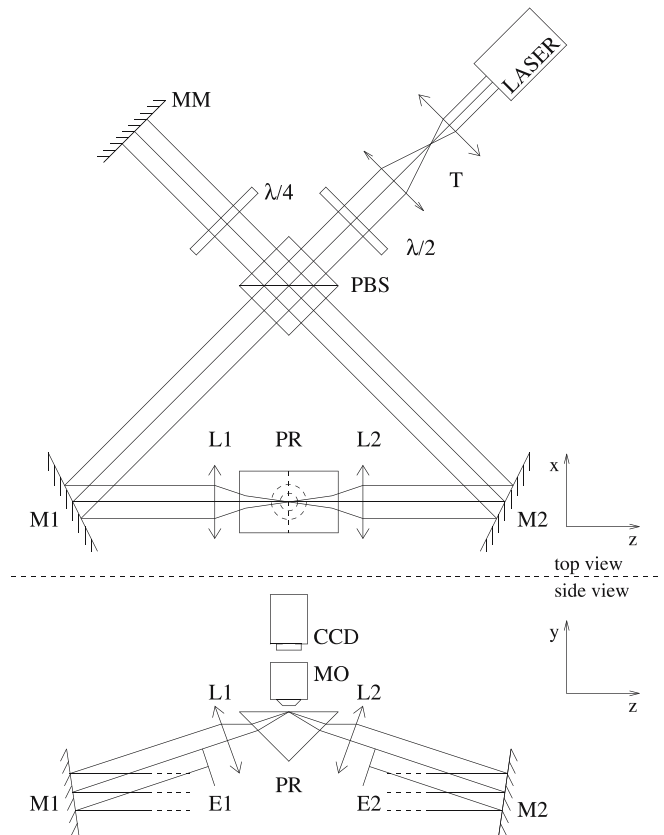


FIGURE 6 Experimental setup. A linearly polarized beam (Verdi, 5 W, $\lambda_{\text{vac}} = 532 \text{ nm}$) is $3\times$ enlarged on passing through the telescope T. The following half-wave plate $\lambda/2$ rotates the polarization so that the beam is separated into two parts. One is reflected on the polarizing beam splitter (PBS), changed to circularly polarized on the $\lambda/4$ plate, reflected on the movable mirror MM, and changed to a linearly polarized beam after passing again through the $\lambda/4$ plate. Its polarization is now perpendicular to the original one reflected to this arm, and so the beam passes through the PBS to the mirror M2 and is focused by lens L2 on the surface of the prism PR made of BK7 glass. The second beam passed through the PBS, the mirror M1, and the lens L1 and overlapped on the top surface of the prism PR with the first beam. The lower plot shows the side view with the edges E1 and E2 we used to block the major part of the beam that formed the propagating wave transmitted through the prism. Therefore, the evanescent field was generated mainly by the high intensity core of the Gaussian beam impinging close to the critical angle 61.92° on the prism top surface. The power of each beam behind the edge was equal to 1.15 W. Overlapping of both beams gave an elliptical spot $40 \mu\text{m}$ long and $10 \mu\text{m}$ wide with standing wave fringes separated by 200 nm. A movable mirror MM was controlled by a PIFOC (Physik Instrumente) which provided fast movement over $150 \mu\text{m}$ very precisely

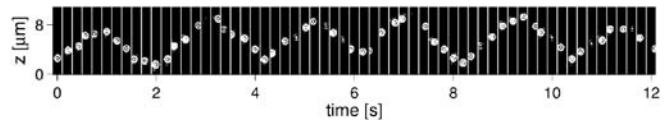


FIGURE 7 Optical delivery of a polystyrene bead of radius 100 nm. The *images* show light scattered by the bead in different times

a method described in [28] and we obtained a resolution of 43.8 nm/pixel . Figure 9 shows a histogram of bead positions along z axis. We assumed a Boltzmann distribution of particle positions [30] and we fitted a function

$$f(z_\psi) = a \exp \left[-\Delta U \sin^2(z_\psi - b) / (k_B T) \right], \quad (30)$$

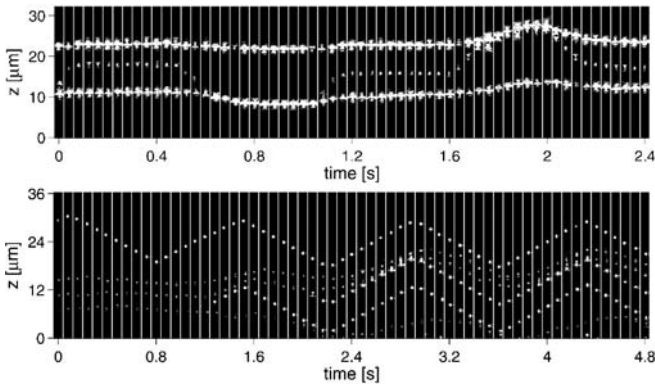


FIGURE 8 Upper figure: record of two polystyrene beads of radius 375 nm (bigger ones) and one polystyrene bead of radius 175 nm. Periods of evanescent standing wave (ESW) motion in both directions are alternated by a period of no ESW motion. The smaller bead follows accurately, the motion of the ESW (if moved) but the bigger one is much less influenced by the ESW in motion. Lower figure: beads of radii 205 nm and 260 nm in a saw-tooth motion of the ESW. This time the bigger beads are much more sensitive to the ESW motion while the smaller ones are remained intact until the bigger ones forced them to move (right part of the record)

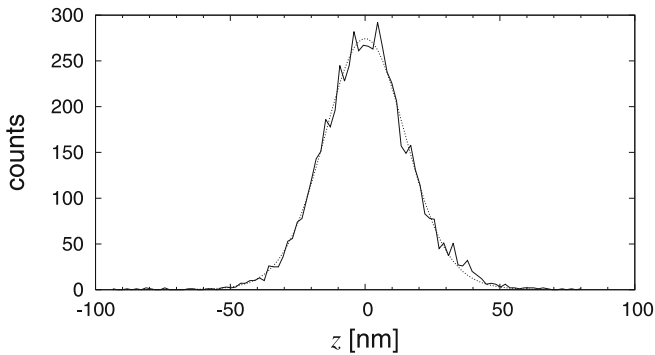


FIGURE 9 Histogram of the position of a bead captured in a standing wave trap. Noisy line shows experimental data of the z coordinate and the smooth line shows a fit by a Gaussian curve. The radius of the polystyrene bead is 260 nm

to the measured histogram with unknown parameters a , ΔU , b and fixed values of temperature T , Boltzmann constant k_B and known phase positions $-\pi \leq z_\psi \leq \pi$ with respect to the bottom of the trap; the sine term reflects the sinusoidal periodicity of the field along z axis. These positions were taken from the periodicity of the scattered object images along the z axis with respect to the standing wave and shifted to the interval $(-\pi, \pi)$. Coincidence between the fit and the data is shown in Fig. 9. It gave us the depth of the optical trap $\Delta U = (9.0 \pm 0.4) k_B T$.

Furthermore, the saw-tooth voltage was applied to the PI-FOC and the moveable mirror moved at a speed v_{ESW} . The bead movement was again recorded by the fast camera with a sampling frequency of 6120 fps. Figure 10 shows the position of the particle (full line) and displacement of its trap site at $t = 0$ (dotted line) if the ESW moved with two velocities. The tracking of the particle in two motional and stationary measurements was performed with the same particle within 20 min. From the values shown in Fig. 10 we calculated the average speeds of the confined particles $v_1 = (44 \pm 4) \mu\text{m s}^{-1}$ and $v_2 = (35 \pm 7) \mu\text{m s}^{-1}$, and also the speed of the ESW movement $v_{\text{ESW}1} = 47 \mu\text{m s}^{-1}$ and $v_{\text{ESW}2} = 98 \mu\text{m s}^{-1}$, respectively. The velocities were calculated as a mean value

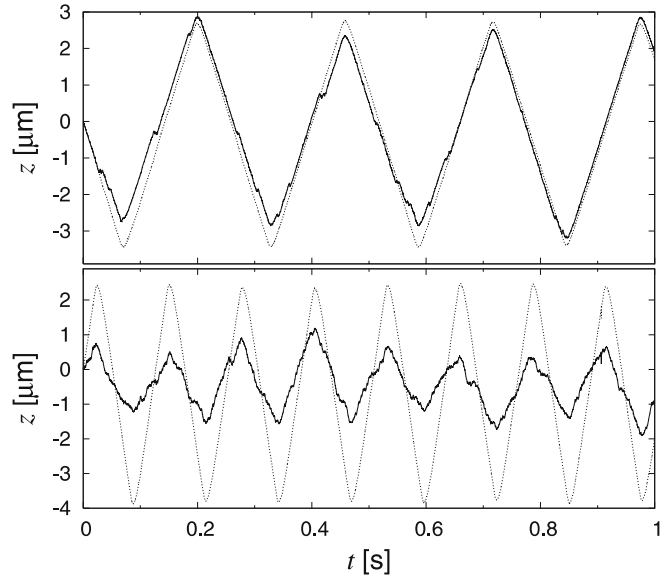


FIGURE 10 Record of bead position while moving a standing wave at different speeds. The solid noisy lines shows the position of the bead during movement and the dotted saw-tooth curves show the displacement of the original bead position at $t = 0$. The upper plot corresponds to a slower ESW motion ($47 \mu\text{m s}^{-1}$) and the lower plot to $98 \mu\text{m s}^{-1}$

from a linear fit to each forward and backward part of the particle movement. One can see, that for bigger v_{ESW} a particle does not follow ESW motion and jumps between neighboring optical traps (so called “Brownian swimmer” [31]). Since our detection method enables precise determination of the bead position with respect to the ESW nodes and antinodes (even in motion) we analyzed this particle position, especially in motional ESW. Figure 11 shows a histogram of bead position if ESW is moved. By fitting (30) we obtained trap

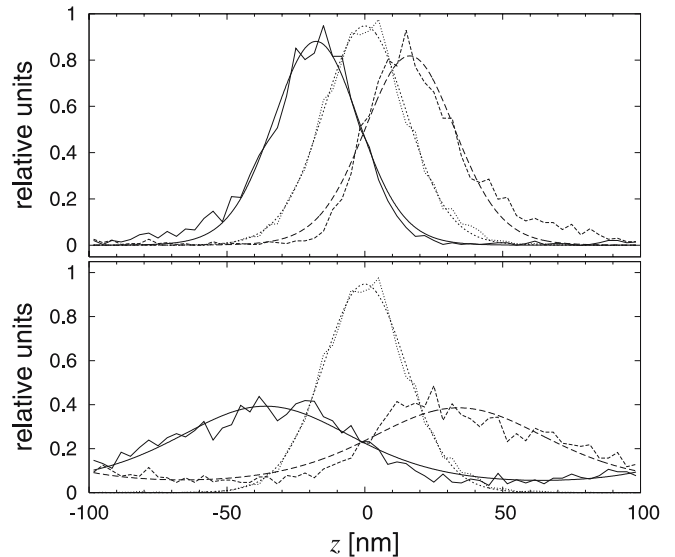


FIGURE 11 Histograms of bead center positions in a slowly (top) and a fast (bottom) moving ESW. Full line is a histogram obtained from the movement of the bead from left to right, dashed line is a histogram of the reversed movement and the dotted line shows a histogram of the bead position with the ESW at rest (from Fig. 9). Smooth curves show a fit of the histogram by a function (30)

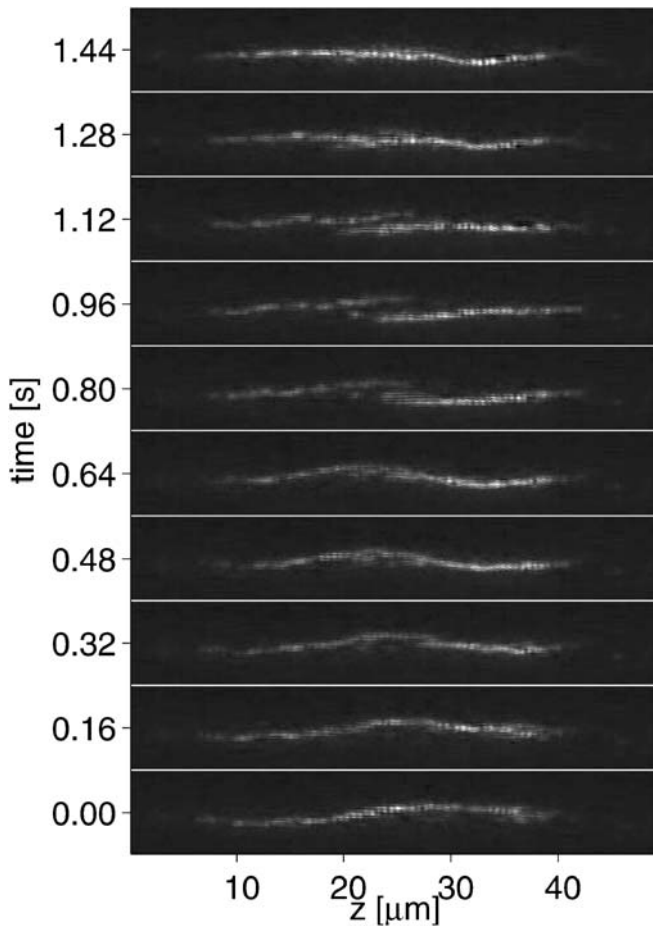


FIGURE 12 Simultaneous confinement of many polystyrene beads of radius 175 nm in an evanescent standing wave

depths $\Delta U_1^{\rightarrow} = (8.5 \pm 0.7) k_B T$ and $\Delta U_1^{\leftarrow} = (7.7 \pm 0.8) k_B T$ for a bead trapped in a slowly moving ESW from the left to the right (ΔU_1^{\rightarrow}) and for the reversed movement (ΔU_1^{\leftarrow}). Similarly we obtained trap depths $\Delta U_2^{\rightarrow} = \Delta U_2^{\leftarrow} = (1.9 \pm 0.2) k_B T$ for fast motion of the ESW. The width of the distribution (30) is equal to $k_B T / \Delta U$. The parameter b in (30) gives the phase deviation of the most populated position from the trap center. Converted to physical displacement Δz we obtain $\Delta z_1^{\rightarrow} = (-17.7 \pm 0.6)$ nm and $\Delta z_1^{\leftarrow} = (16 \pm 1)$ nm for a slowly moving ESW, $\Delta z_2^{\rightarrow} = (-36 \pm 2)$ nm and $\Delta z_2^{\leftarrow} = (34 \pm 3)$ nm for a fast moving ESW, respectively. Small velocities v_{ESW} cause only small deviations from the equilibrium position while bigger velocities of the ESW cause more frequent jumps between neighboring traps accompanied by a wider histogram, i.e. a lower trap depth, and a bigger particle displacement from the equilibrium position compared to a slowly moving ESW.

More than one bead can be confined in an array of optical traps created by ESW. The inter bead interactions increase with the number of confined beads, a part of this interaction is via rescattering of the trapping beam – optical binding [32, 33]. Figure 12 shows examples of experimental confinement of polystyrene beads of radius 175 nm into ESW. Large amounts of beads are trapped forming an elastic array [34] that is synchronously bent due to Brownian motion and mutual interaction between the particles [28, 35]. The

linear chain of particles often breaks into two or more separate parts that are, within a fraction of a second, again unified in the single chain. Over the course of time some particles join the chain while other particles are ejected (usually after chain breaks). The amplitude of the lateral displacement and frequency of the chain breaks grow with increasing numbers of beads in the chain. Similar self-organization of beads into a linear chain was observed even if both counter-propagating evanescent waves had perpendicular polarizations. The distances between beads were again regular but depending on the bead size.

4 Conclusions

We have presented a theoretical model that enables calculation of the optical forces acting on nano and micro-particles placed into an interference field created by several evanescent waves. We have applied this theory to the case of two counter-propagating evanescent waves, and shown how the maximal optical force along the standing wave depends on the particle diameter and angle of incidence of the plane waves on the solid–liquid interface. We have compared the results obtained by Rayleigh approximation and by Lorentz–Mie scattering theory. Agreement to within 10% was obtained for bead radii $a < \lambda/20$ (wavelength in liquid), i.e. for bead radii smaller than 20 nm. We proved that there are certain bead radii that are not affected by the standing wave because no axial force coming from the evanescent standing wave (ESW) acts on these beads. We have also shown that the amplitude of the force along the standing wave decreases with growing incident angle, but that bead radii insensitivity to the evanescent standing wave stays the same for all studied angles. The basic idea of sub-micron particle confinement into the ESW was proved using polystyrene beads of radius 100 nm. By changing the phase of one beam these beads were delivered in a motional ESW over a distance of 5 μm . The alternating dependence on the object size was proven experimentally where certain bead sizes were not sensitive to the ESW motion. We also studied experimentally, how the velocity of the ESW influences the behavior of delivering beads using our original detection method [28], this is especially useful for the determination of particle position with respect to the standing wave in motion. We obtained average velocities of particle movement for different speeds of ESW, and full understanding of this problem will be useful for rectification of Brownian motion and its use in Brownian motors. Counter-propagating, interfering, and even non-interfering beams allowed confinement of many beads which were formed into a linear chain, and we observed the elastic behavior, ruptures, and self-repair of this chain.

ACKNOWLEDGEMENTS We thank Prof. Kishan Dholakia and Dr. Veneranda Garcés-Chávez for stimulating discussions. This work was partially supported by the EC 6FP NEST Adventure Activity (ATOM3D, project No. 508952), ISI IRP (AV0Z20650511), GA AS CR (IAA1065203), and MEYS CR (LC06007).

REFERENCES

- 1 T. Esslinger, M. Weidemüller, A. Hemmerich, T.W. Hansch, *Opt. Lett.* **18**, 450 (1993)
- 2 D. Pohl, W. Denk, M. Lanz, *Appl. Phys. Lett.* **44**, 651 (1984)
- 3 N. Fang, H. Lee, C. Sun, X. Zhang, *Science* **308**, 534 (2005)

- 4 M.J. Lang, S.M. Block, *Am. J. Phys.* **71**, 201 (2003)
- 5 S. Kawata, T. Sugiura, *Opt. Lett.* **17**, 772 (1992)
- 6 S. Kawata, T. Tani, *Opt. Lett.* **21**, 1768 (1996)
- 7 T. Tanaka, S. Yamamoto, *Appl. Phys. Lett.* **77**, 3131 (2000)
- 8 M. Gu, J.B. Haumonte, Y. Micheau, J.W.M. Chon, X. Gan, *Appl. Phys. Lett.* **84**, 4236 (2004)
- 9 V. Garcés-Chávez, K. Dholakia, G.C. Spalding, *Appl. Phys. Lett.* **86**, 031 106 (2005)
- 10 R. Quidant, D. Petrov, G. Badenes, *Opt. Lett.* **30**, 1009 (2005)
- 11 L. Novotny, R.X. Bian, X.S. Xie, *Phys. Rev. Lett.* **79**, 645 (1997)
- 12 K. Okamoto, S. Kawata, *Phys. Rev. Lett.* **83**, 4534 (1999)
- 13 P. Chaumet, A. Rahmani, M. Nieto-Vesperinas, *Phys. Rev. Lett.* **88**, 123 601 (2002)
- 14 P. Zemánek, A. Jonáš, L. Šrámek, M. Liška, *Opt. Commun.* **151**, 273 (1998)
- 15 P. Zemánek, C.J. Foot, in *Wave and Quantum Aspects of Contemporary Optics: Proc. SPIE*, Vol. 3320, ed. by J. Nowak, M. Zajac (1998), pp. 97–103
- 16 I. Dotsenko, W. Alt, M. Khudaverdyan, S. Kuhr, D. Meschede, Y. Miroshnychenko, D. Schrader, A. Rauschenbeutel, *Phys. Rev. Lett.* **95**, 033 002 (2005)
- 17 T. Čižmár, V. Garcés-Chávez, K. Dholakia, P. Zemánek, *Appl. Phys. Lett.* **86**, 174 101 (2005)
- 18 P. Zemánek, V. Karásek, A. Sasso, *Opt. Commun.* **240**, 401 (2004)
- 19 E. Almaas, I. Brevik, *J. Opt. Soc. Am. B* **12**, 2429 (1995)
- 20 S.R. de Groot, L.G. Suttrop, *Foundations of Electrodynamics* (North Holland, Amsterdam, 1971)
- 21 P. Chaumet, M. Nieto-Vesperinas, *Opt. Lett.* **25**, 1065 (2000)
- 22 Y. Harada, T. Asakura, *Opt. Commun.* **124**, 529 (1996)
- 23 B. Draine, *Astrophys J.* **333**, 848 (1988)
- 24 J.P. Barton, D.R. Alexander, S.A. Schaub, *J. Appl. Phys.* **66**, 4594 (1989)
- 25 P. Zemánek, A. Jonáš, M. Liška, *J. Opt. Soc. Am. A* **19**, 1025 (2002)
- 26 P. Zemánek, A. Jonáš, P. Jákł, M. Šerý, J. Ježek, M. Liška, *Opt. Commun.* **220**, 401 (2003)
- 27 P. Jákł, M. Šerý, J. Ježek, A. Jonáš, M. Liška, P. Zemánek, *J. Mod. Opt.* **50**, 1615 (2003)
- 28 T. Čižmár, M. Šiler, M. Šerý, P. Zemánek, V. Garcés-Chávez, K. Dholakia, Arxiv: <http://arxiv.org/abs/physics/0509054> (2005)
- 29 M. Gu, P.C. Ke, *Appl. Phys. Lett.* **75**, 175 (1999)
- 30 E.L. Florin, A. Pralle, E.H.K. Stelzer, J.K.H. Horber, *Appl. Phys. A* **66**, 75 (1998)
- 31 P. Reimann, *Phys. Rep.* **361**, 57 (2002)
- 32 S.A. Tatarkova, A.E. Carruthers, K. Dholakia, *Phys. Rev. Lett.* **89**, 283 901 (2002)
- 33 W. Singer, M. Frick, S. Bernet, M. Ritsch-Marte, *J. Opt. Soc. Am. B* **20**, 1568 (2003)
- 34 J.P. Pantina, E.M. Furst, *Phys. Rev. Lett.* **94** (2005)
- 35 C.D. Mellor, C.D. Bain, *Chem. Phys. Chem.* **7**, 329 (2006)